Journal of Materials Chemistry A

Energy-Distinguishable Bipolar UV Photoelectron Injection from LiCl-Promoted $FAPbCl_3$ Perovskite Nanorods

Journal:	*Journal of Materials Chemistry A*
Manuscript ID	TA-ART-01-2019-001160.R2
Article Type:	Paper
Date Submitted by the Author:	24-Mar-2019

Complete List of Authors:	Gong, Jue ; Northern Illinois University, Department of Chemistry and Biochemistry Li, Xun; Northern Illinois University, Department of Chemistry and Biochemistry Guo, Peijun; Argonne National Laboratory, Center for Nanoscale Materials Zhang, Ian; Northern Illinois University, Department of Chemistry and Biochemistry Huang, Wei; Northwestern University, Department of Chemistry; Northwestern University, Materials Research Center Lu, Ke; Northern Illinois University, Department of Chemistry and Biochemistry Cheng, Yingwen; Northern Illinois University, Department of Chemistry and Biochemistry Schaller, Richard; Argonne National Laboratory, Center for Nanoscale Materials; Northwestern University, Department of Chemistry Marks, Tobin; Northwestern University, Department of Chemistry; Northwestern University, Materials Research Center Xu, Tao; Northern Illinois University, Department of Chemistry and Biochemistry

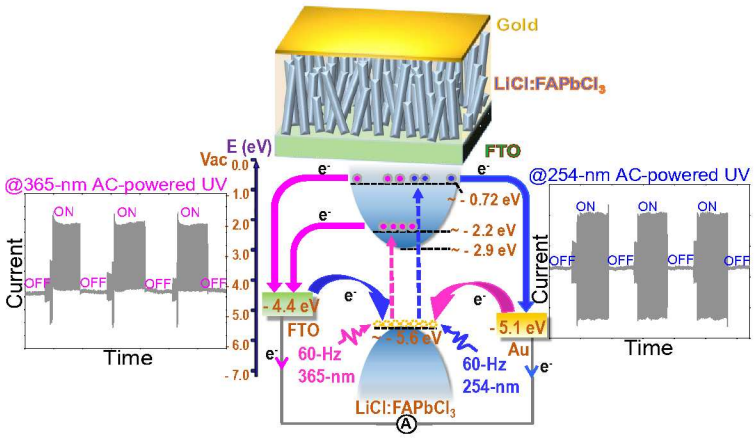

Textual abstract: UV photodetector based on LiCl-added $FAPbCl_3$ nanorods exhibits bipolar photocurrent under 60-Hz 254-nm UV illumination. However, under 60-Hz 365-nm UV irradiation, LiCl:$FAPbCl_3$ nanorods show monopolar photocurrent.

ARTICLE

Energy-Distinguishable Bipolar UV Photoelectron Injection from LiCl-Promoted $FAPbCl_3$ Perovskite Nanorods

Received 00th January 2019,
Accepted 00th January 2019

DOI: 10.1039/x0xx00000x

Jue Gong,[a] Xun Li,[a] Peijun Guo,[b] Ian Zhang,[a] Wei Huang,[cd] Ke Lu,[a] Yingwen Cheng,[a] Richard D. Schaller,[bc] Tobin J. Marks[cd] and Tao Xu*[a]

High-performance optoelectronic devices, such as solar cells and light-emitting diodes, have been fabricated on lead halide perovskites owing to their superior carrier properties. However, charge transports in such optoelectronics are intrinsically directional due to the existence of p-n junctions, which thus lacks any potential to elucidate any perturbations in light or electricity during energy conversion. Here, with the presence of LiCl additive in formamidinium chloride (FACl) solution, as-grown LiCl:$FAPbCl_3$ nanorods demonstrated greatly enhanced crystllinity and UV photoresponse as compared to pristine $FAPbCl_3$ nanostructures without LiCl additive. Most importantly, LiCl:$FAPbCl_3$ nanorod film exhibits unprecedented distinguishability to UV photons with different energies and oscillating intensities, as in the form of bipolar and periodically oscillatory photocurrents. This work could advance the fundamental understanding of photoinduced carrier processes in halide perovskites and facilitate the development of novel UV-based optical communications.

Introduction

Ultraviolet (UV) radiation has given rise to high-speed, wide-coverage and non-line-of-sight wireless optical communications due to its small susceptibility to solar background interference and flexibility of transmitter/receiver orientations such as pointing, acquisition and tracking.[1-4] For a wireless UV communication, function generator produces pattern-controlled electrical signals that contain characteristic information on the intensity and on-off frequency of UV photons, which are emitted by transmitter and subsequently detected by receiver to realize the relay of information.[2,5] Moreover, UV radiations with different wavelengths are employed in communication systems so as to enable bidirectional and high-capacity optical transmission, where large distinction between UV wavelengths is demanded for minimized inter-channel interference.[2,6] Therefore, developing a photodetector that can accurately identify UV intensity variation, while simultaneously distinguishing UV photons in different wavelengths is highly desirable for acquiring and decoding the information embedded in UV carriers. Owing to the suitable bandgaps and superior charge transport properties, lead halide perovskites (e.g. $MAPbCl_3$, $CsPbCl_3$, $FAPbI_3$) have realized high-performance UV photodetectors.[7-14] Nonetheless, such photodetectors were never able to differentiate UV photons with different energies due to indiscriminate, unidirectional transport of photogenerated charge carriers in 1) prototypical p-i-n photodiode structures,[7,8] 2) lateral photoconductor structures with external voltage biases,[9,12-14] and 3) devices utilizing metal electrodes with much discrepant work functions for guided carrier migration.[10] In addition, photodetectors need to be sufficiently sensitive to accurately detect UV photons with temporally varying intensities based on superior photoelectronic properties (e.g. large free carrier density, high mobility), since optical information can also be ciphered in the oscillating intensities. As such, it is intriguing both at scientific and technological levels to develop UV photodetector that permits multidirectional carrier transport in perovskite materials with radically improved optoelectronic properties, so as to observe perturbed photocurrent responses and to eventually elucidate the energies and intensities of UV photons. Herein, through lithium chloride (LiCl, 1 mg/mL) additive mixed in formamidinium chloride (FACl, 10 mg/mL)/isopropanol solution, synthesized formamidinium lead chloride ($FAPbCl_3$) nanorods (detailed methods elaborated in Supporting Information (SI)) exhibited significantly improved crystallinity and enhanced photoresponse upon 365-nm UV illumination (powered by direct current (DC)), in comparison with the pristine $FAPbCl_3$ nanostructures grown without LiCl additive. In the meantime, high-crystallinity LiCl-promoted $FAPbCl_3$ (LiCl:$FAPbCl_3$) nanorod film displayed sensitive distinguishability between alternating current (AC) powered 254-nm and AC powered 365-nm UV illuminations with oscillatory light intensities via periodically damping and bipolar photocurrents.

Results and discussion

X-ray diffraction (XRD) was first performed to characterize the structural properties of as-synthesized LiCl:$FAPbCl_3$ and $FAPbCl_3$ nanostructures. As shown in Fig. 1a, solution-grown LiCl:$FAPbCl_3$

[a] Department of Chemistry and Biochemistry, Northern Illinois University, DeKalb, IL 60115, USA. E-mail: txu@niu.edu
[b] Center for Nanoscale Materials, Argonne National Laboratory, Argonne, IL 60439, USA.
[c] Department of Chemistry, Northwestern University, 2145 Sheridan Road, Evanston, IL 60208, USA.
[d] Materials Research Center, Northwestern University, 2145 Sheridan Road, Evanston, IL 60208, USA.

† Electronic Supplementary Information (ESI) available. See DOI: 10.1039/x0xx00000x

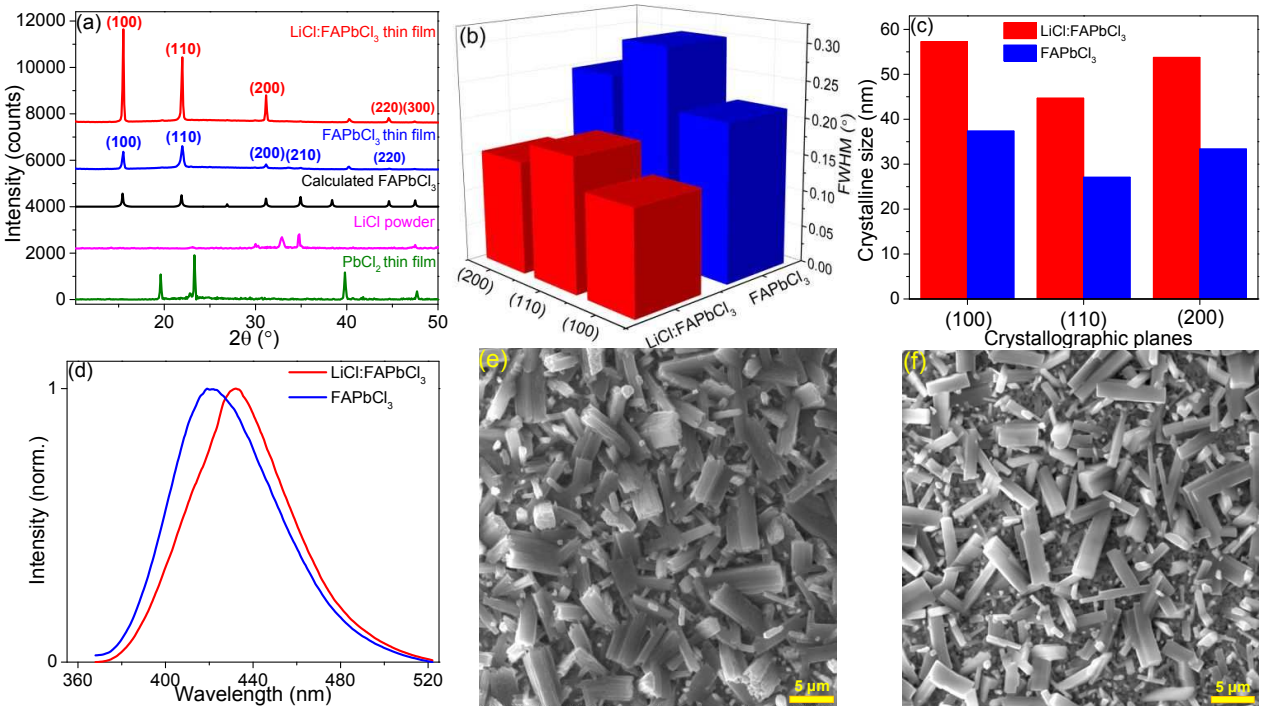

Fig. 1 Crystallinity analysis of pristine $FAPbCl_3$ and LiCl:$FAPbCl_3$ nanostructured films. (a) XRD patterns of $FAPbCl_3$ nanostructures grown with LiCl additive (red), without LiCl additive (blue), reported $FAPbCl_3$ (black) by Govinda et al.[15], $PbCl_2$ (green) and LiCl (magenta) precursors. (b) FWHMs of pristine $FAPbCl_3$ (blue) and LiCl:$FAPbCl_3$ (red). (c) Summary of crystalline sizes for (100), (110) and (200) crystallographic planes. (d) Fluorescence spectra of LiCl:$FAPbCl_3$ (red) and pristine $FAPbCl_3$ (blue). SEM images of pristine $FAPbCl_3$ (e) and LiCl:$FAPbCl_3$ (f) nanostructures under 5.21-kx magnification.

nanostructured film (red trace) displays diffraction peaks of (100), (110) and (200) planes with much greater intensities in contrast with $FAPbCl_3$ counterpart (blue trace). Quantitatively, the large peak intensity ratios—~5.4, ~2.9, ~7.6 for (100), (110), (200) planes respectively, prove the greater crystallinity of LiCl:$FAPbCl_3$ relative to $FAPbCl_3$. Also, the preferred crystallographic orientations on LiCl:$FAPbCl_3$ is notably changed relative to pristine $FAPbCl_3$, which agrees well with the fact that additives/dopants can effectively alter materials' microstructures.[16-18] The XRD patterns on both perovskite $FAPbCl_3$ films closely match the reported pattern (black),[15] and therefore indicate a complete reaction of $PbCl_2$ (green) and LiCl (magenta) precursors. Structural refinement of LiCl:$FAPbCl_3$ film reveals an enlarged cell parameter (~5.8505 Å) in contrast with the reported 5.7379 Å, thereby indicating the doping of Li^+ in material lattice, as shown in Fig. S1. X-ray photoelectron spectroscopy (XPS) unambiguously confirms the existence of Li^+ within the LiCl:$FAPbCl_3$ nanorods, along with the constituent C, N, Pb and Cl elements, as shown in Fig. S2. From the XPS study, Pb to Li atomic ratio is calculated to be ~1.6 (Table S2).

Detailed analysis of the diffraction peaks reveals notably smaller FWHMs on LiCl:$FAPbCl_3$ film (Fig. 1b), thereby signifying much larger crystalline sizes[19] of $FAPbCl_3$ nanostructures grown with LiCl additive than the pristine $FAPbCl_3$ counterpart, as verified on (200), (110) and (100) orientations (Fig. 1c) through Scherrer's equation—$D=k\lambda/b\text{Cos}\theta$,[20-22] in which D, k, λ, b and θ respectively represent crystallite size, shape factor (0.9), wavelength of X-ray photons (1.54 Å for Cu Kα radiation), FWHM and diffraction angle. Additionally, LiCl:$FAPbCl_3$ clearly exhibits a fluorescence with redshifted peak intensity at 432 nm (Fig. 1d) with respect to pristine $FAPbCl_3$ at 420 nm. The distinctively narrowed optical bandgap has once again corroborated the enhanced crystallinity in perovskite materials.[23-25] Also, FWHM of LiCl:$FAPbCl_3$ fluorescence peak (~53 nm) is smaller than pristine $FAPbCl_3$ (~57 nm), which implies a more homogeneous band structure on LiCl:$FAPbCl_3$ as due to the crystallinity improvement. Explicitly, LiCl:$FAPbCl_3$ nanowires display highly ordered morphology as featured with sharp edges and flat end facets on micrometre-size crystals, in contrast with pristine $FAPbCl_3$ nanostructures that are much more disordered in shapes, as shown in Figs 1 e & f. From the chemistry perspectives, the higher crystallinity of LiCl:$FAPbCl_3$ nanorods stems from the dissolution and recrystallization process (Ostwald ripening)[26-29] as caused by the large concentration of Cl^- from LiCl additive (see SI Methods section for details). This claim can be validated by $FAPbCl_3$ that is grown from high-concentration FACl precursor (~12 mg/mL, contains equivalent amount of Cl^- as in LiCl:$FAPbCl_3$), which also exhibits significantly stronger (100) and (200) orientations (Fig. S3) than $FAPbCl_3$ with 10 mg/mL FACl precursor (Fig. 1a blue) and thus signifies its much higher crystallinity. In the meantime, addition of Li^+ selectively helps to improve the crystallinity of resulting $FAPbCl_3$ nanorods through (110) orientation, as compared with the greatly suppressed (110) plane in high-concentration FACl-promoted $FAPbCl_3$ (Fig. S3), agreeing well with K^+ doping reported previously.[30,31] To validate the feasibility for UV photodetector, optical reflectance was subsequently performed on pristine $FAPbCl_3$ nanostructured film, where the amount of light reflected quickly falls as photon wavelength goes below 400 nm (Fig. S4), thereby indicating the large absorption of UV photons and the

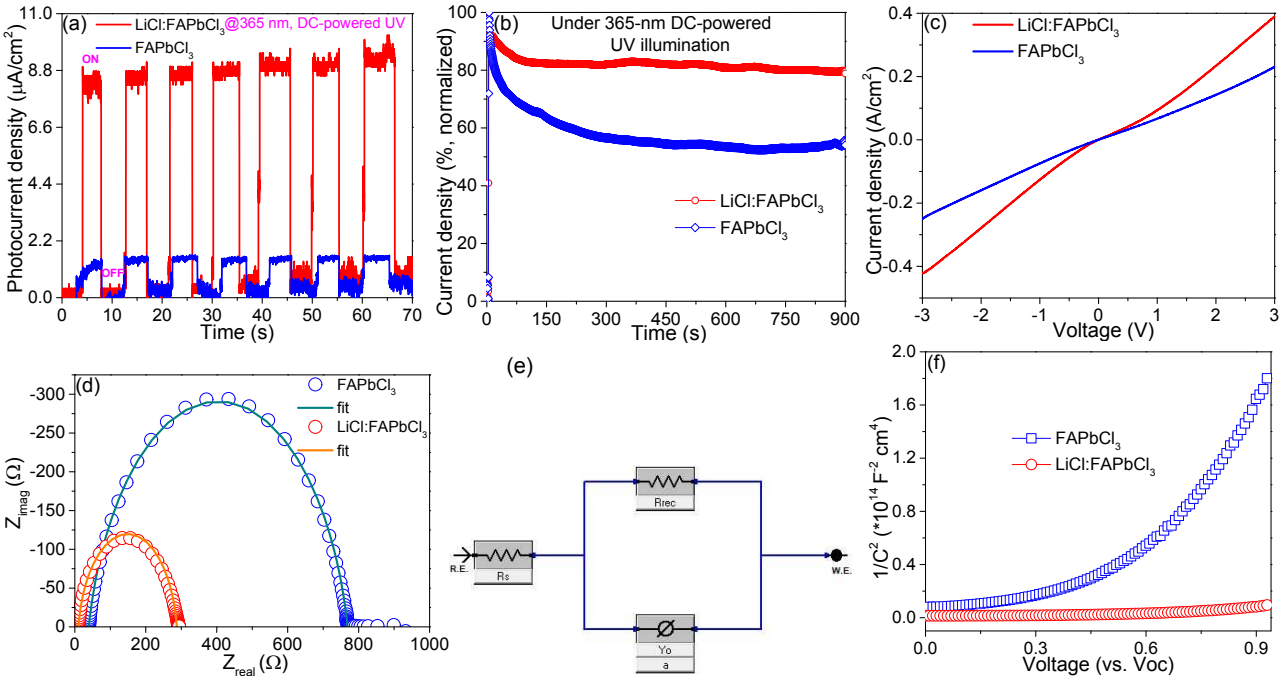

Fig. 2 UV photoresponse and electrical characterizations of LiCl:$FAPbCl_3$ (red) and pristine $FAPbCl_3$ (blue) nanostructured films. On-off photocurrents of LiCl:$FAPbCl_3$-based (red) and $FAPbCl_3$-based (blue) photodetectors under DC-powered 365-nm UV illumination (a), photostability plots of pristine $FAPbCl_3$ (blue) and LiCl:$FAPbCl_3$ (red) nanostructured films under continuous illumination of DC-powered 365-nm UV light (b). Dark currents were subtracted to align the baselines of LiCl:$FAPbCl_3$ and $FAPbCl_3$ photodetectors in (a). (c) Linear sweep voltammogram of perovskite films measured in dark condition. (d) Nyquist plots of perovskite films under DC-powered 365-nm UV illumination. (e) Equivalent circuit applied in fitting the impedance curves shown in (d). (f) Mott-Schottky plots of perovskite films measured under DC-powered 365-nm UV illumination.

consequent generation of photoelectrons. Indeed, as shown in Fig. 2a, upon on-off switching of 365-nm UV illumination, both pristine $FAPbCl_3$ and LiCl:$FAPbCl_3$ photodetectors (fabrication methods elaborated in SI) show functional photocurrent response. Nevertheless, LiCl:$FAPbCl_3$ film exhibits remarkably larger photocurrent densities at around 9 μA/cm^2 in contrast with 1.6 μA/cm^2 on pristine $FAPbCl_3$, which accounts for more than 5-fold increase and therefore demonstrates the greatly enhanced optoelectronic performance as due to LiCl-induced crystallinity improvement. Detailed studies of the rise and decay behaviours of single on-off current cycles show much faster rising kinetics on LiCl:$FAPbCl_3$ photodetector over the $FAPbCl_3$ counterpart, as shown in Fig. S5, and thus signifies a greater photoelectric sensitivity on LiCl:$FAPbCl_3$ photodetector. Comparatively, as shown in Table S2, responsivities of LiCl:$FAPbCl_3$ (~167 mA/W) and $FAPbCl_3$ (~29 mA/W) photodetectors are notably greater than devices based on ZnO thin film (0.1 mA/W)[32], $LiNbO_3$ single crystal (17.1 mA/W)[33], $LiTaO_3$ single crystal (2 mA/W)[34] and $LaAlO_3$ single crystal (71.8 mA/W)[35]. It thus indicates the promising suitability of LiCl:$FAPbCl_3$ and $FAPbCl_3$ in UV detection. Synergistically, the improved crystallinity on LiCl:$FAPbCl_3$ also led to outstandingly enhanced photostability, in which LiCl:$FAPbCl_3$ retained ~80% of its original photocurrent density after 900 seconds of continuous UV illumination while pristine $FAPbCl_3$ exhibited <60% retention of its initial current density, as shown in Fig. 2b. Accordingly, what accounts for the enhanced photoelectric performance of LiCl:$FAPbCl_3$ nanostructured film are its notably improved charge transport kinetics. It is unambiguous to see that LiCl:$FAPbCl_3$ had exceptionally increased electrical conductivity (Fig. 2c) and much smaller electrochemical impedance (Fig. 2d) as compared to pristine $FAPbCl_3$ counterpart. By adopting a common resistance//capacitance (R//C) circuit model for metal/perovskite/metal constructions[36,37] as shown in Fig. 2e, the charge recombination resistances (R_{rec}), chemical capacitances (constant phase element, CPE) as well as the electron transit times (R_{rec}*CPE) were calculated and summarized in Table 1. The fact that LiCl:$FAPbCl_3$ exhibited shorter electron lifetime (0.000150 s) than pristine $FAPbCl_3$ (0.00144 s) implies its exceptionally greater carrier mobility[38].

Table 1. Summary of R_{rec}, CPE and time constants obtained from the electrochemical impedance fittings in Fig. 2d.

Perovskite film	R_{rec} (Ω)	CPE (F)	Lifetime (s)
$FAPbCl_3$	729.6	$1.97*10^{-6}$	0.00144
LiCl:$FAPbCl_3$	276.9	$5.41*10^{-7}$	0.000150

As shown in Fig. 2f, Mott-Schottky plots further suggest that LiCl:$FAPbCl_3$ had remarkably greater free carrier density ($1.98*10^{17}$/cm^3) in contrast to pristine $FAPbCl_3$ ($1.03*10^{16}$/cm^3), as evidenced by its much smaller voltage-dependent curve slope via the following equation:[39,40]

$$N_c = \frac{2}{e_0 \varepsilon \varepsilon_0 [\frac{\partial \left(\frac{1}{C^2}\right)}{\partial V}]^{-1}}$$

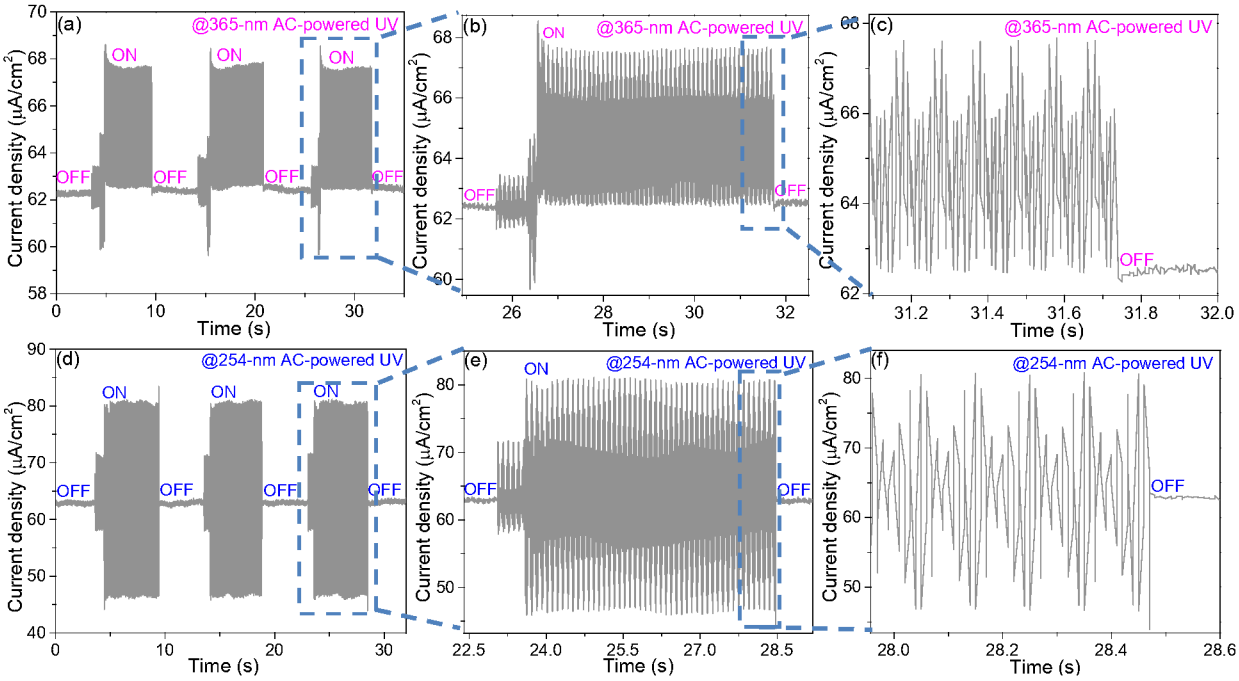

Fig. 3 Time-dependent UV photoresponse of perovskite photodetectors. On-off photocurrents of LiCl:$FAPbCl_3$-based photodetector under 365-nm AC-powered UV illumination (a), 254-nm AC-powered UV illumination (d), zoomed-in views of the 365-nm UV photocurrent signals (b, c), and 254-nm photocurrent signals (e, f).

where N_c, e_0, ε, ε_0 and $[\partial(1/C^2)/\partial V]$ stands for carrier concentration, electron charge ($1.602*10^{-19}$ C), dielectric constant (≈30 for pristine $FAPbCl_3$ at room temperature)[15], vacuum permittivity ($8.854*10^{-12}$ F/m) and slope of Mott-Schottky plot, respectively.

Importantly, abovementioned photoresponse was achieved with UV light source powered by batteries (UVL-4F UV lamp, picture shown in Fig. S6), which therefore operated on constant current and UV light intensity. This is verified by Fourier transform (FT) of LiCl:$FAPbCl_3$ on-off photocurrents (Fig. S7), where no frequency components are found and therefore signify the absence of periodically oscillating photocurrents. Nevertheless, in the presence of a AC-powered 60-Hz 365-nm UV illumination (UVGL-25, picture shown in Fig. S8), LiCl:$FAPbCl_3$ exhibited photocurrents with oscillating magnitudes (Figs 3 a - c), which is on par with the oscillatory nature of UV light intensity and implies a highly sensitive photoelectronic response of LiCl:$FAPbCl_3$-based device. Moreover, by performing FT of the observed chronoamperogram, distinctive frequency components—60-Hz, 120-Hz, 180-Hz and 240-Hz are witnessed, as shown in Fig. S9, which thus indicates that photocurrents were periodically oscillating and closely echoes the 60-Hz current oscillation frequency of 365-nm UV light source (Fig. S8). Astonishingly, under 254-nm AC-powered UV illumination, LiCl:$FAPbCl_3$ detector unexpectedly shows current signals both above and below the dark current, and hence suggests that the UV-induced photoelectron injection was temporally switching directions, as shown in Figs 3 d - f.

The periodically damping nature of 60-Hz 254-nm photocurrents is once again confirmed by FT coefficient plot of the observed chronoamperogram. Similarly, frequency-domain coefficient plots clearly show the existence of 60-Hz frequency component, which is characteristic of 120-Hz, 180-Hz and 240-Hz harmonic current frequencies (Fig. 4) and again closely corroborates the 60-Hz current/light intensity oscillation frequency (Fig. S8). Vitally, by quantitatively analyzing the FT coefficient plots of 60-Hz 365-nm/254-nm photocurrents (Fig. S9 and Fig. 4), one can find that the magnitudes of coefficients under 254-nm UV are much greater than the 365-nm counterparts. Moreover, 365-nm-induced photocurrents have a frequency distribution between 100 and 150 Hz that is comparable with the frequency distributions in the ranges of 50-75 Hz and 175-200 Hz. This frequency profile, however, is evidently different from 254-nm FT coefficients, which have very small frequency compositions in the range of 100-150 Hz and at 240 Hz (Figs 4 c, d & e). The perturbed frequency components can be valuably exploited in future optical communications, as information can be effectively ciphered and decoded through modulated amplitude, frequency and also the phase of current.

Furthermore, the temporal direction switching of photoelectron injection under 60-Hz 254-nm UV is unique to the demonstrated LiCl:$FAPbCl_3$ photodetector. Through chronoamperometry studies on a commercial Si photodiode with lateral interdigitated electrodes, we found that 60-Hz 254-nm UV photons did not give rise to any bipolar photoelectron injections, as manifested by the photocurrent signals that are one-sided to the background dark currents, although the benchmark Si photodiode is also capable of sensitively detecting the AC-powered 254-nm and 365-nm UV photons via periodically oscillatory currents (Figs S10 and S11). The indifferent photoresponse of Si photodiode under 254-nm and 365-nm irradiations implies the absence of distinguishability toward UV photons with different energies in regular device architecture with interdigitated electrodes. Substantially, the back electron transfer under 60-Hz 254-nm UV is further validated through chronopotentiometry studies, where LiCl:$FAPbCl_3$ demonstrates

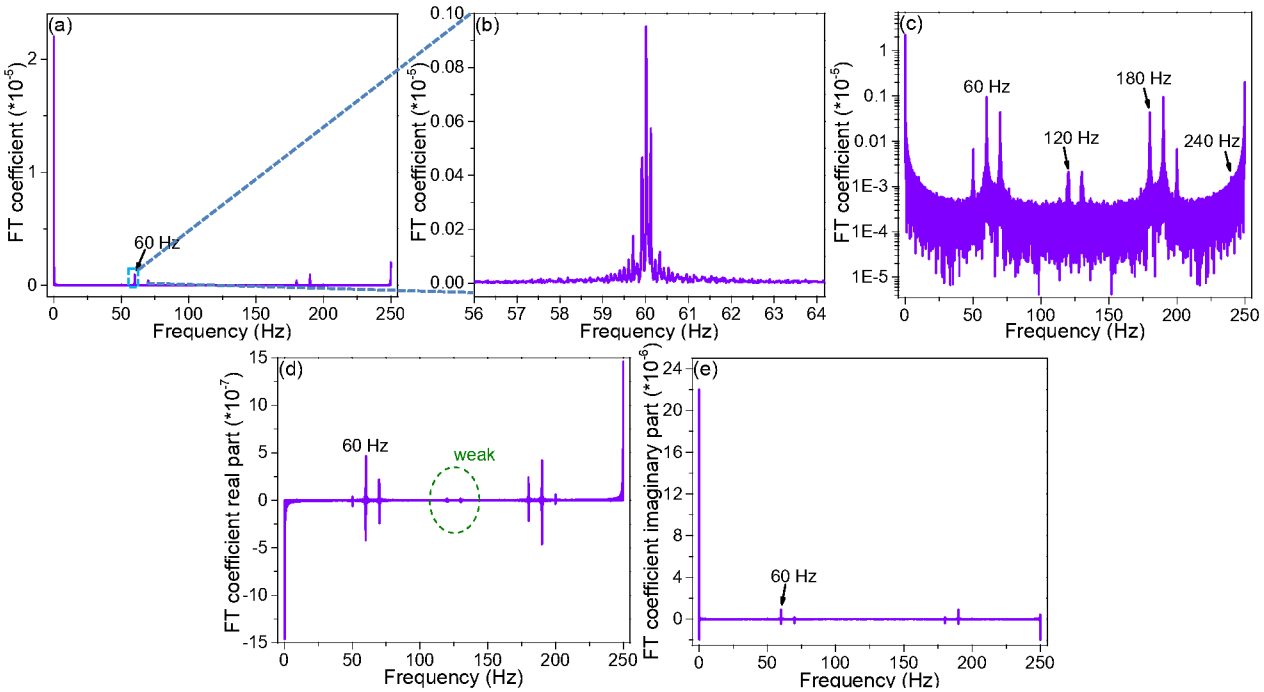

Fig. 4 FT of the chronoamperogram measured under 60-Hz 254-nm UV as shown in Fig. 3d for LiCl:FAPbCl$_3$ nanostructured film. (a) FT coefficient plot. (b) Zoomed-in view of the coefficient plot in the range of 56 to 64 Hz. (c) Logarithmic scale of coefficient plot. (d) and (e) Real-part and imaginary-part coefficient plots, respectively.

bipolar photovoltage signals with respect to the background V_{oc} under the 254-nm AC-powered UV illumination; meanwhile, 365-nm AC-powered UV photons led to on-off photovoltage signals that are one-sided to the V_{oc}, as shown in Fig. S12.

To account for the photophysical origin of bipolar photoresponses under 60-Hz 254-nm UV photons, UV-Vis absorbance was subsequently performed on LiCl:FAPbCl$_3$ nanostructured pellet. As shown in Fig. S13a, absorbance at 254 nm (1.878) and 365 nm (0.179) leads to a ratio of corresponding absorption coefficients of ~10.5 according to Beer-Lambert's equation:

$$A = \alpha c l$$

in which α, c and l stand for absorption coefficient, density and thickness of material, respectively. Under average optical power densities of 60-Hz 254-nm (0.007532 mW/cm^2) and 365-nm (0.008517 mW/cm^2), the difference in absorption coefficients therefore results in 254-nm photoelectrons that are 6 times in number over the 365-nm photoelectrons. Explicitly, the large number of 254-nm photoelectrons is manifested in the large responsivity (~1.54 A/W) and photocurrent magnitude that is nearly 4 times over the photocurrent achieved under 365-nm AC-powered UV, as shown in Fig. S13b. It is noteworthy that the photocurrent densities summarized in Fig. S13b are average magnitudes in order to be on par with the average optical power densities measured by a light meter (LI-250A), via the following equation due to their sinusoidally oscillating nature:

$$J_{avg} = \frac{2J_p}{\pi}$$

where J_p and J_{avg} respectively represent peak and average photocurrent densities. Fundamentally, it is the large concentration of 254-nm-induced photocarriers in the conduction band of LiCl:FAPbCl$_3$ that enables bipolar electron injections, where electrons selectively flow toward FTO side at the beginning of 254-nm UV illumination due to the much scarcer density of states in FTO than that in metallic gold, which can be clearly perceived from the semi-metallic nature[41,42] of FTO. After FTO is fully saturated with electrons, migration of photoelectrons will switch to gold side, with the whole charge transfer process repeating reciprocally between the two electrodes, as illustrated in Fig. 5, where the energy levels of valence band maximum and conduction band minimum are determined by ultraviolet photoelectron spectroscopy (Fig. S14) and optical bandgap (~2.7 eV, Fig. S13a). Additionally, absorbance spectrum of LiCl:FAPbCl$_3$ (Fig. S13a) distinctively reveals an onset area (between 350-500 nm) that is smoothly followed by a drastic rise of absorbance below 350 nm, which was unforeseen on other perovskite materials[43-48] and implies an exponentially increased conduction band states (greater bandwidths) at higher energy levels. The

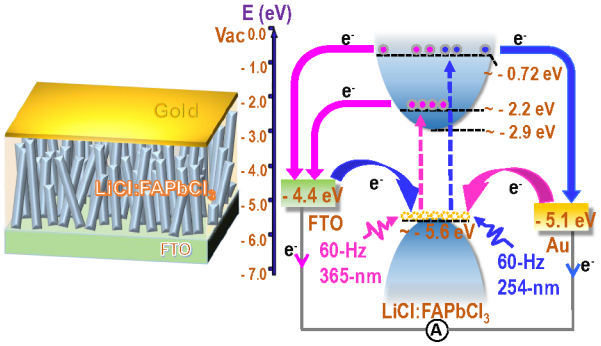

Fig. 5 Schematic illustration of energy band diagram and migration of photoexcited electrons (right) in FTO/LiCl:FAPbCl$_3$/Au device (left) under 365-nm and 254-nm AC-powered UV illuminations.

significantly greater bandwidth at higher energy in conduction band allows to accommodate more photoelectrons excited by 254-nm UV light, and thus greatly augments the probability of bipolar photoelectron injections as compared with photoelectrons excited under 365-nm UV.

Conclusions

In summary, we conducted chronoamperometry studies of high-crystallinity LiCl:FAPbCl$_3$ nanostructured photodetector, where it exhibits prominent distinguishability towards AC-powered 365/254 nm UV illuminations in the way of periodically oscillating and bipolar photoelectron injections into FTO and Au electrodes. On-off photovoltages further verify the observed current polarities on LiCl:FAPbCl$_3$ device. Fundamentally, the photophysical origin of observed bipolar photoresponse under AC-powered 254-nm UV illumination lies in the large number and wide conduction bandwidth of 254-nm excited photoelectrons. From the structural perspectives, the highly ordered morphology and directional alignment of LiCl:FAPbCl$_3$ nanorods help to guide the massive number of 254-nm excited photoelectrons towards charge collection electrodes, thereby suppressing the noise current. The demonstrated bipolar photoresponse provides an additional dimension to cipher and decipher information, in addition to the conventionally adopted amplitude and frequency modulations. Also, with different charge collection electrodes and meticulous band structure engineering, we can correspondingly tune the energy levels of photodetectors to distinguish more UV wavelengths. Our work will significantly contribute to the development of UV-based optical communications and perovskite optoelectronics with novel functionalities.

Conflicts of interest

There are no conflicts to declare.

Acknowledgements

T.X. acknowledges support from the U.S. National Science Foundation (DMR-1806152). Part of this work was performed at the Center for Nanoscale Materials, a U.S. Department of Energy Office of Science User Facility, and supported by the U.S. Department of Energy, Office of Science, under Contract No. DE-AC02-06CH11357. W.H. and T.J.M. acknowledge the support from Northwestern University MRSEC (DMR-1720139). Ian Zhang is a summer high school student volunteer from Naperville Neuqua Valley High School. J.G. acknowledges the experiment support from Prof. Elizabeth R. Gaillard.

Notes and references

1 M. Z. Chowdhury, M. T. Hossan, A. Islam and Y. M. Jang, *IEEE Access*, 2018, **6**, 9819-9840.
2 Z. Xu and B. M. Sadler, *IEEE Commun. Mag.*, 2008, **46**, 67-73.
3 X. Sun, Z. Zhang, A. Chaaban, T. K. Ng, C. Shen, R. Chen, J. Yan, H. Sun, X. Li, J. Wang, J. Li, M.-S. Alouini and B. S. Ooi, *Opt. Express*, 2017, **25**, 23267-23274.
4 H. Qin, Y. Zuo, D. Zhang, Y. Li and J. Wu, *Opt. Express*, 2017, **25**, 5018-5030.
5 Z. Xu, G. Chen, F. Abou-Galala and M. Leonardi, *Proc. SPIE*, 2007, **6709**, 67090Y.
6 T.-f. Zhao, A.-l. Zhang and R.-l. Xue, *Optoelectron. Lett.*, 2013, **9**, 208-212.
7 L. Dou, Y. (M.) Yang, J. You, Z. Hong, W.-H. Chang, G. Li and Y. Yang, *Nat. Commun.*, 2014, **5**, 5404.
8 M. Zhang, F. Zhang, Y. Wang, L. Zhu, Y. Hu, Z. Lou, Y. Hou and F. Teng, *Sci. Rep.*, 2018, **8**, 11157.
9 Q. Han, S.-H. Bae, P. Sun, Y.-T. Hsieh, Y. (M.) Yang, Y. S. Rim, H. Zhao, Q. Chen, W. Shi, G. Li and Y. Yang, *Adv. Mater.*, 2016, **28**, 2253-2258.
10 G. Maculan, A. D. Sheikh, A. L. Abdelhady, M. I. Saidaminov, M. A. Haque, B. Murali, E. Alarousu, O. F. Mohammed, T. Wu and O. M. Bakr, *J. Phys. Chem. Lett.*, 2015, **6**, 3781-3786.
11 W. Deng, L. Huang, X. Xu, X. Zhang, X. Jin, S.-T. Lee and J. Jie, *Nano Lett.*, 2017, **17**, 2482-2489.
12 Z. Zhang, W. Zheng, R. Lin and F. Huang, *R. Soc. open Sci.*, 2018, **5**, 180905.
13 W. Wang, H. Xu, J. Cai, J. Zhu, C. Ni, F. Hong, Z. Fang, F. Xu, S. Cui, R. Xu, L. Wang, F. Xu and J. Huang, *Opt. Express*, 2016, **24**, 8411-8419.
14 J. Zhang, Q. Wang, X. Zhang, J. Jiang, Z. Gao, Z. Jin and S. (F.) Liu, *RSC Adv.*, 2017, **7**, 36722-36727.
15 S. Govinda, B. P. Kore, D. Swain, A. Hossain, C. De, T. N. G. Row and D. D. Sarma, *J. Phys. Chem. C*, 2018, **122**, 13758-13766.
16 Y. Yang, Y. Jin, H. He, Q. Wang, Y. Tu, H. Lu and Z. Ye, *J. Am. Chem. Soc.*, 2010, **132**, 13381-13394.
17 J. T. Wang, X. L. Shi, W. W. Liu, X. H. Zhong, J. N. Wang, Pyrah, L., K. D. Sanderson, P. M. Ramsey, M. Hirata and K. Tsuri, *Sci. Rep.*, 2014, **4**, 3679.
18 C. Zhou, Y. Tian, O. Khabou, M. Worku, Y. Zhou, J. Hurley, H. Lin and B. Ma, *ACS Appl. Mater. Interfaces*, 2017, **9**, 40446-40451.
19 G. Liu, J. Gong, L. Kong, R. D. Schaller, Q. Hu, Z. Liu, S. Yan, W. Yang, C. C. Stoumpos, M. G. Kanatzidis, H.-k. Mao and T. Xu, *Proc. Natl. Acad. Sci. U.S.A.*, 2018, **115**, 8076-8081.
20 M. Soleymani and M. Edrissi, *Bull. Mater. Sci.*, 2016, **39**, 487-490.
21 L. Zaraska, K. Mika, K. E. Hnida, M. Gajewska, T. Lojewski, M. Jaskula and G. D. Sulka, *Mater. Sci. Eng. B*, 2017, **226**, 94-98.
22 R.-G. Ciocarlan, E. M. Seftel, M. Mertens, A. Pui, M. Mazaj, N. N. Tusar and P. Cool, *Mater. Sci. Eng. B*, 2018, **230**, 1-7.
23 N. J. Jeon, J. H. Noh, W. S. Yang, Y. C. Kim, S. Ryu, J. Seo and S. I. Seok, *Nature*, 2015, **517**, 476-480.
24 M. I. Saidaminov, A. L. Abdelhady, G. Maculan and O. M. Bakr, *Chem. Commun.*, 2015, **51**, 17658-17661.
25 T. M. Koh, K. Fu, Y. Fang, S. Chen, T. C. Sum, N. Mathews, S. G. Mhaisalkar, P. P. Boix and T. Baikie, *J. Phys. Chem. C*, 2014, **118**, 16458-16462.
26 M. Yang, T. Zhang, P. Schulz, Z. Li, G. Li, D. H. Kim, N. Guo, J. J. Berry, K. Zhu and Y. Zhao, *Nat. Commun.*, 2016, **7**, 12305.
27 X. Cao, L. Zhi, Y. Li, F. Fang, X. Cui, L. Ci, K. Ding and J. Wei, *ACS Appl. Energy Mater.*, 2018, **1**, 868-875.
28 Y. Fu, F. Meng, M. B. Rowley, B. J. Thompson, M. J. Shearer, D. Ma, R. J. Hamers, J. C. Wright and S. Jin, *J. Am. Chem. Soc.*, 2015, **137**, 5810-5818.
29 H. Zhu, Y. Fu, F. Meng, X. Wu, Z. Gong, Q. Ding, M. V. Gustafsson, M. T. Trinh, S. Jin and X-Y. Zhu, *Nat. Mater.*, 2015, **14**, 636-642.
30 T. Bu, X. Liu, Y. Zhou, J. Yi, X. Huang, L. Luo, J. Xiao, Z. Ku, Y. Peng, F. Huang, Y.-B. Cheng and J. Zhong, *Energy & Environ. Sci.*, 2017, **10**, 2509-2515.
31 X. Liu, Y. Zhang, L. Shi, Z. Liu, J. Huang, J. S. Yun, Y. Zeng, A. Pu, K. Sun, Z. Hameiri, J. A. Stride, J. Seidel, M. A. Green and X. Hao, *Adv. Energy Mater.*, 2018, **8**, 1800138.

32 J. H. Jun, H. Seong, K. Cho, B.-M. Moon and S. Kim, *Ceram. Int.* 2009, **35**, 2797-2801.
33 E.-J. Guo, J. Xing, K.-J. Jin, H.-B. Lu, J. Wen and G.-Z. Yang, *J. Appl. Phys.* 2009, **106**, 023114.
34 E.-J. Guo, J. Xing, H.-B. Lu, K.-J. Jin, J. Wen and G.-Z. Yang, *J. Phys. D* 2009, **43**, 1.
35 J. Xing, E. Guo, K.-j. Jin, H. Lu, J. Wen and G. Yang, *Opt. Lett.* 2009, **34**, 1675-1677.
36 Y. C. Kim, K. H. Kim, D.-Y. Son, D.-N. Jeong, J.-Y. Seo, Y. S. Choi, I. T. Han, S. Y. Lee and N.-G. Park, *Nature*, 2017, **550**, 87-91.
37 H. Wang, J. Huang, S. Xing and J. Yu, *Org. Electron.*, 2016, **28**, 11-19.
38 G. Hodes, *J. Phys. Chem. Lett.*, 2015, **6**, 4090-4092.
39 C. Yang, Z. Wang, T. Lin, H. Yin, X. Lu, D. Wan, T. Xu, C. Zheng, J. Lin, F. Huang, X. Xie and M. Jiang, *J. Am. Chem. Soc.*, 2013, **135**, 17831-17838.
40 M. G. Walter, E. L. Warren, J. R. McKone, S. W. Boettcher, Q. Mi, E. A. Santori and N. S. Lewis, *Chem. Rev.*, 2010, **110**, 6446-6473.
41 Z. Yang, S. Gao, T. Li, F.-Q. Liu, Y. Ren and T. Xu, *ACS Appl. Mater. Interfaces*, 2012, **4**, 4419-4427.
42 M. Turrion, B. Macht, H. Tributsch and P. Salvador, *J. Phys. Chem. B*, 2001, **105**, 9732-9738.
43 L. Kong, G. Liu, J. Gong, Q. Hu, R. D. Schaller, P. Dera, D. Zhang, Z. Liu, W. Yang, K. Zhu, Y. Tang, C. Wang, S.-H. Wei, T. Xu and H.-k. Mao, *Proc. Natl. Acad. Sci. U.S.A.*, 2016, **113**, 8910-8915.
44 Y. Zhou, M. Yang, W. Wu, A. L. Vasiliev, K. Zhu and N. P. Padture, *J. Mater. Chem. A*, 2015, **3**, 8178-8184.
45 W. Ke, G. Fang, J. Wan, H. Tao, Q. Liu, L. Xiong, P. Qin, J. Wang, H. Lei, G. Yang, M. Qin, X. Zhao and Y. Yan, *Nat. Commun.*, 2015, **6**, 6700.
46 T. M. Koh, V. Shanmugam, X. Guo, S. S. Lim, O. Filonik, E. M. Herzig, P. Müller-Buschbaum, V. Swamy, S. T. Chien, S. G. Mhaisalkar and N. Mathews, *J. Mater. Chem. A*, 2018, **6**, 2122-2128.
47 J. Chen, X. Lian, Y. Zhang, W. Yang, J. Li, M. Qin, X. Lu, G. Wu and H. Chen, *J. Mater. Chem. A*, 2018, **6**, 18010-18017.
48 M. Wang, B. Li, P. Siffalovic, L.-C. Chen, G. Cao and J. Tian, *J. Mater. Chem. A*, 2018, **6**, 15386-15394.